Patricia Termain Eliason
Laurence A. Soderblom
Pat S. Chavez, Jr.
U.S. Geological Survey
Flagstaff, AZ 86001

Extraction of Topographic and Spectral Albedo Information from Multispectral Images

The process is a completely closed system employing only the image data, and can be applied to any digital multispectral data set.

Abstract: *A computer technique has been developed to separate and extract spectral-reflectivity variations and topographic information from multispectral images. The process is a completely closed system employing only the image data and can be applied to any digital multispectral data set. An unsupervised cluster analysis based solely on the relative spectral properties (color and brightness) is performed on an image, using multispectral ratios. The average brightness of values whose color ratios cluster together is taken to represent a single material of uniform color and albedo. The average brightness of the cluster is taken as the predicted brightness of all picture elements in the cluster if the surface were flat. An estimate of the scene modulation due to topography only is then derived by simply dividing the original image by the predicted brightnesses, were the surface flat. Further data reduction can produce uncalibrated albedo maps for all wavelength bands. These maps, essentially free of topography but including both brightness and spectral information (monotonic maps with albedo), can be used in either supervised or unsupervised classification. The topographic modulation component can be integrated to produce a digital pseudo-topography (local, relative height) that provides subjectively correct stereo-perception.*

Introduction

Images of light reflected from a solid surface, in general, contain two kinds of information: (1) spectral-reflectivity variations related to the intrinsic properties (albedo and color) of materials within the scene, and (2) reflected-intensity variations due to slope or topography that modulate the illuminating flux that is incident on the surface. In the absence of albedo and color variation, image brightness is a function of topography only. In such a case, knowledge of the photometric function of the surface should, in principle, allow derivation of the topography, a process called photoclinometry. Most studies using this technique have involved the Moon, whose surface is relatively uniform in regard to materials, albedo, and color. These studies, which combined photometric models with photographic and photoelectric photometry and some photogrammetry, refined the technique. Mathematical foundations and operational theories were developed for the method, and extended the theory to include surfaces whose photometric functions do not possess the special degeneracy of the lunar case (Hapke, 1963, 1966; Wildey and Pohn, 1964, 1969; Watson, 1968; Lucchitta and Gambell, 1969; Rowan *et al.*, 1971; Wildey, 1971, 1975; Bonner and Schmall, 1973). The success of such studies was only marginal except for certain specialized surfaces; even at best, photoclinometry is limited by fundamental mathematical concepts. However, the primary culprit was the confusion of albedo variations over a wide range of scales with topographically induced brightness variations, even for a surface as simple as that of the Moon. Because photoclinometry involves integration of slopes esti-

Photogrammetric Engineering and Remote Sensing,
Vol. 48, No. 11, November 1981, pp. 1571-1579.

0099-1112/81/4711-1571$02.25/0

mated from local brightnesses, and because the previous studies employed only black-and-white images, albedo variations were hopelessly confused with local incidence angle variations in computing the topographic profiles.

Compared with earlier concepts of photoclinometry (developed either for the Moon or the general case), that of the present investigation described here is heuristic and simplified. The primary difference in our approach is that we separate the image into brightness variations due to topography and brightness variations due to the intrinsic spectral reflectance of the materials, by using multispectral classification techniques. The classification of the relative spectral properties, using multispectral ratios, provides a good estimate of the average scene brightness and eliminates the confusion between albedo and insolation variations.

In order that the two types of information can be separated, we assume that modulation of scene brightness due to topography is, to the first order, independent of material properties and wavelength, i.e., we assume that all materials have the same photometric function at close wavelengths. In general, this assumption is obviously not true, but because the average slopes at the scale of resolution of the images utilized are gentle (less than a few degrees), it is a good first-order approximation. Further, we assume that the photometric function is independent of wavelength, also a reasonable approximation over a narrow range of slopes. The ultimate justification for these assumptions is manifested in the final results. Assuming these approximations, we next describe how the two types of information are separable by use of multispectral data.

General Theory

An image (image brightness-distribution) as viewed by a camera system from space can be defined as a function in a two-dimensional space. The amount of light, B, reflected from a small portion of the surface at position (x,y) is a function of the photometric function, ϕ, and of the albedo, a, such that

$$B(x,y) = f(x,y,\phi)\, a(x,y). \tag{1}$$

The expression can be expanded to the following form:

$$B(x,y,\lambda) = R(x,y,\lambda) * M_T(T(x,y), \phi(\alpha,i,\epsilon)) + H(\lambda). \tag{2}$$

The spectral reflectivity, R, is the product of the solar flux and the two-way transmission of the atmosphere. $R(x,y,\lambda)$ is the brightness of the scene as a function of wavelength, λ, if the surface were flat. M_T is the modulation of the brightness introduced by topography; it is a function of the topography, $T(x,y)$, and the photometric function $\phi(\alpha,i,\epsilon)$. The value of the photometric function, in turn, depends upon the phase angle, α, the incidence angle, i, and the angle of emergence, ϵ (Wildey, 1975). The angles of incidence and emergence allow for an unambiguous definition of the viewing and lighting geometry.

The additive atmospheric scattering effects are defined by $H(\lambda)$, and are due primarily to molecular scattering. They are a function of wavelength (e.g., Rayleigh scattering is inversely proportional to the fourth power of the wavelength, λ^{-4}, and Mie scattering is inversely proportional to wavelength at a range of exponents from 0 to -4). Several studies have derived $H(\lambda)$ directly from the Landsat data; generally an average solution is used (Chavez, 1975). Multiplicative atmospheric effects inherent in $H(\lambda)$ (reflection, absorption, transmission) are all wavelength dependent and included in R.

After subtracting the average atmospheric scattering, $H(\lambda)$, the brightness distribution in the image becomes

$$B = R * M_T. \tag{3}$$

Using this equation as the basis for this study, the next step is to independently derive R. For this process we employ an unsupervised clustering technique that is applied to the relative spectral properties of the image, using selected multispectral ratios. The average brightness values of image picture elements (pixels) whose ratios cluster together is taken to represent R for their respective clusters. A map of R is then produced. Two basic assumptions are inherent in this technique: (1) all image elements that group in a ratio cluster represent a single material with uniform color or albedo (materials with the same albedo have the same color); and (2) the slopes of all elements in a color cluster are symmetrically distributed toward and away from the sun, such that their average brightness can be used to estimate the brightness of that material on a flat surface (to linearize the photometric function over a narrow range of slopes). The limitations that these assumptions place on the results are discussed later. For simplicity, we further assume that the lighting and viewing geometry is unambiguous (i.e., the angle directions in space are constant) and that atmospheric scattering over the scene is uniform. Once an estimate of R is obtained, it is divided into the image already corrected for haze (Equation 3) to derive an estimate of M_T, which is in turn used to derive a digital pseudo-topography, by employing a model photometric function.

Computation

Landsat Multispectral Scanner (MSS) digital data and Viking Orbiter multispectral vidicon digital data were used for this study. Characteristics of the Landsat data are described in various reports,

including those of the National Aeronautics and Space Administration (1976) and Taranik (1978). The Landsat MSS system measures light reflected from the Earth in four wavelength bands in the visible and near infrared (Band 4, 0.5 to 0.6 micrometres; Band 5, 0.6 to 0.7 micrometres; Band 6, 0.7 to 0.8 micrometres; and Band 7, 0.8 to 1.1 micrometres). Information on the Viking Orbiter 1975 Mars imaging experiment is documented by Benesh and Thorpe (1976). Viking Orbiter measurements were made in three spectral bands (as well as clear), using a combination of narrow-band spectral filters and neutral density filters that obtain nearly constant vidicon output current (Violet, 0.42 to 0.48 micrometres; Green, 0.48 to 0.58 micrometres; and Red, 0.54 to 0.64 micrometres). Although only these two data sets were used in this study, the process can be applied to any multispectral data set.

The computation was separated into two stages: (1) derivation of the average brightness distribution, the synthetic "flat" image $R(x,y,\lambda)$; and (2) extraction of the topographic component, M_T. These stages are described in detail in the following section.

SEPARATION OF THE TOPOGRAPHIC AND SPECTRAL ALBEDO COMPONENTS

Ratios are used in this study as a basis for multispectral classification. Ratioed images are generated by dividing the digital brightness values in one multispectral (*MS*) band by the corresponding values in another band. The ratio of two bands, i and j, after haze correction can be written from Equation 3:

$$r_{ij} = \frac{R(x,y,\lambda_i)}{R(x,y,\lambda_j)} \tag{4}$$

Because we have assumed the photometric function to be independent of wavelength, the ratio does not (in theory) depend on topography but only on material properties. Therefore, the color information in the four Landsat bands can be reduced to three independent ratios. The r_{65} ratio best distinguishes between major material groups (water, soil/rock, vegetation) but has little or no discrimination within group types; the r_{54} ratio best separates units within a soil/rock group; and the r_{76} ratio is best for classification of vegetation types.

We first consider the Landsat data. In order to derive an estimate for $R(x,y,\lambda_i)$, we begin with the three Landsat ratios and band i, 8-bit integer values (256 density numbers (DN)). In principle, we first solve for $\bar{R}_i(r_{54},r_{65},r_{76})$, which is the average brightness of band i of a ratio cluster with ratio coordinates r_{54},r_{65},r_{76}. Using this value, $R(x,y,\lambda_i)$ can be derived from the values of the ratios r_{54},r_{65},r_{76} for each point (x,y) in the image. Unfortunately, the direct computation of such a function for the Landsat data is not feasible with a minicomputer, as it requires an enormous amount of computer memory (256^3, real precision). Storing such a three-dimensional array on a direct-access device such as a "look-up" table and retrieving R for every point is also not feasible because of the tremendous number of input/output accesses. Our solution is to reduce the three Landsat ratios further, to two variables.

The first variable is simply the r_{65} ratio, which best separates vegetation from soils, rocks, and water. The second function is derived by applying a simple weighting scheme to the three band ratios r_{54}, r_{65}, r_{76}. The new variable (r) assumes the value of r_{54} where r_{65} is low or midrange (implying mostly soil and rocks and/or water); it assumes the value of r_{76} where the r_{65} ratio is high (implying mostly vegetation). The function used is

$$r = ((r_{65} - A) * r_{76} + (B - r_{65}) * r_{54}) / (A - B) \tag{5}$$

where A and B are the average values of r_{65} for the two major classes, soil/rock and vegetation, respectively. Landsat band 5, the ratio r_{65}, and the ratio composite r are used as the first example (Figure 1).

This process reduces $\bar{R}_i$ to a function of two variables, $\bar{R}_i(r_{65},r)$, which requires 256^2 (real precision) memory bytes. However, ratios generally do not fill the entire dynamic data range (256 DN), and so can be remapped into 64 DN, requiring only about 10^4 memory bytes. Derivation of $R(x,y,\lambda_i)$ is done in two stages. The first stage derives $\bar{R}_i$ by means of a simple two-dimensional clustering procedure that sums the brightness values of all image points in band i that have the same r_{65} and r values (representing a cluster); the average of each cluster is then computed (Figure 2a). The average brightness is a function of the scatter of brightness values within the cluster (Figure 2b).

The second stage uses $\bar{R}_i$ to compute $R(x,y,\lambda_i)$, by assigning to each pixel the average brightness value R corresponding to that pixel's r_{65} and r values. The result, $R(x,y,\lambda_i)$, is an estimate of the average scene brightness were there no topographic relief (Figure 3).

The topographic modulation expressed in terms of Equation 3 can be rewritten:

$$M_T(T,\Phi) = \frac{B(x,y,\lambda_i)}{R(x,y,\lambda_i)} \tag{6}$$

The synthetic albedo map $R(x,y,\lambda_i)$ is used in the above equation to derive the brightness distribution of M_T, a theoretical image with albedo or color variation eliminated and tonal variation unambiguously identified with slope modulation (Figure 4).

We now consider the less complicated Viking example. The three Viking MS bands can likewise be reduced to two band ratios, red/green (r_{rg}) and

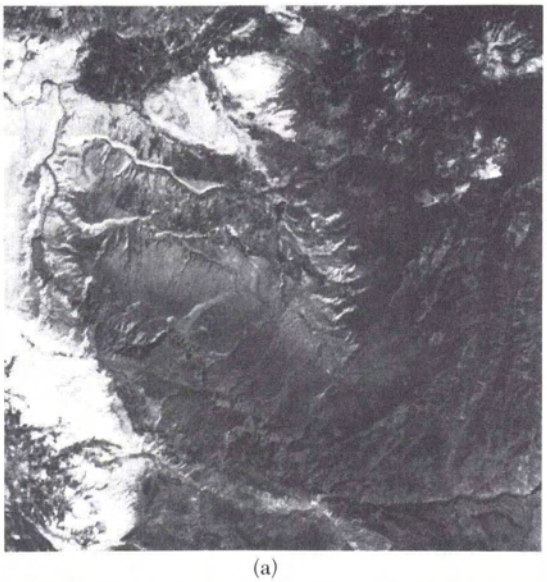

(a)

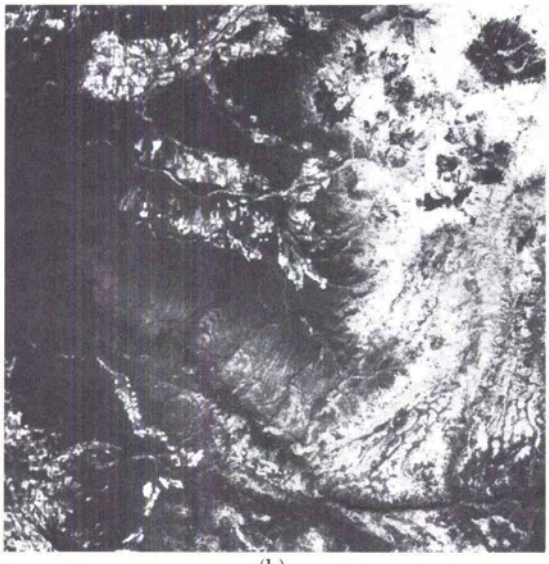

(b)

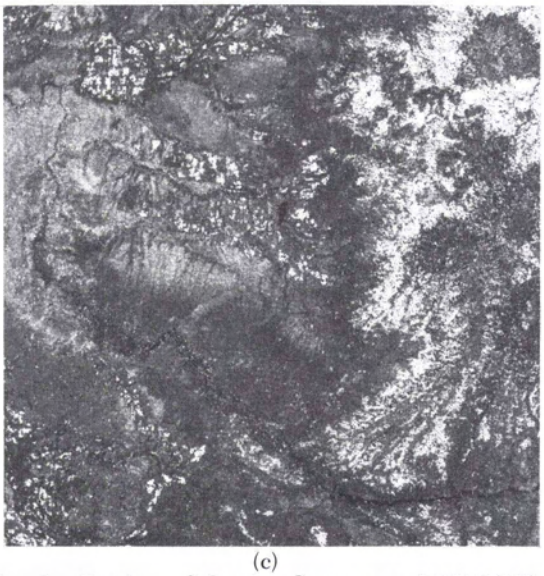

(c)

FIG. 1. Portion of the Landsat scene 1407-17190, showing part of the drainage area of the Gunnison River, Colorado, acquired 13 September 1973. North is at top. Scale is 80 m/pixel. (a) Band 5, used to derive the average brightness values; image array size is 1000 by 1000 pixels. (b) Ratio of bands 6 to 5, used to separate the two major material classes of soil/rock/water and vegetation. (c) Ratio composite r (see text), which best separates variations between the two classes.

violet/green (r_{vg}). The albedo properties of Mars are much less complex than those of Earth. Lack of vegetation limits the spectral reflectivity of surface materials to the soil/rock group. The simpler geology of Mars results in a smaller number of soil and rock units and allows fairly complete separation of materials using the two band ratios. The red band and the two ratios used in this example are shown in Figure 5.

In a manner similar to that described in the preceding Landsat example, $\bar{R}_i(r_{rg},r_{vg})$ is computed for

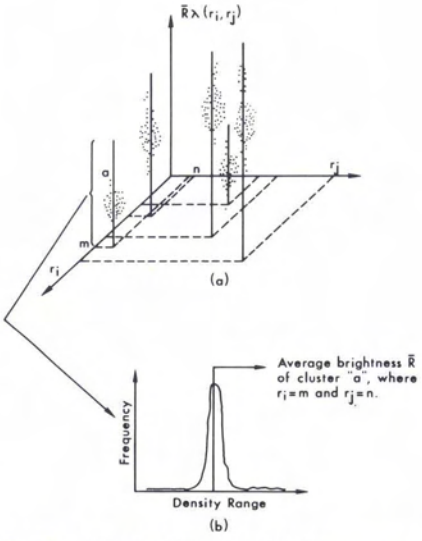

FIG. 2. Cluster Diagram. (a) Diagramatic representation of two-dimensional cluster plot used in the cluster analysis classification. For each cluster, average brightness values (r_i, r_j) are computed and inserted in an image depending upon the (r_i, r_j) of each pixel. (b) One brightness cluster shown diagramatically. The dimension of the cluster and the resultant average brightness are functions of the scatter of values within the cluster.

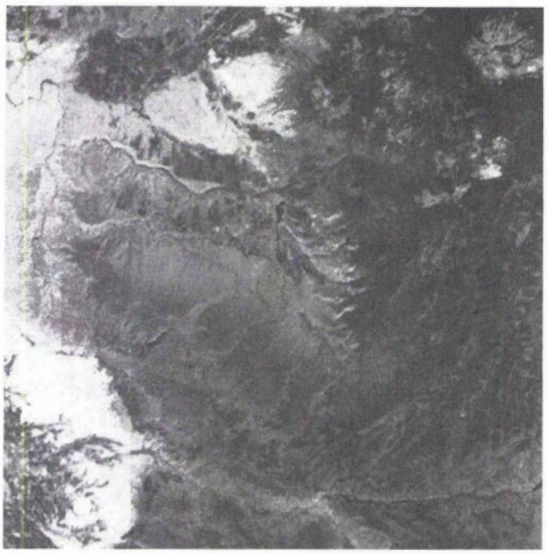

FIG. 3. Image brightness distribution representing an estimate of the average scene brightness, $R(x,y,\lambda_5)$, as if the surface were flat. This image was generated by performing an unsupervised cluster analysis technique on band 5, using multispectral ratios. Landsat scene same as that of Figure 1.

all image points. $\bar{R}_i$, the average brightness, is used to compute $R(x,y,\lambda_i)$, the synthetic "flat" image (Figure 6). The topographic modulation component, M_T, is derived by simply dividing the estimate of the average scene brightness, $R(x,y,\lambda_i)$, into the brightness of the original scene, $B(x,y,\lambda_i)$ (Figure 7).

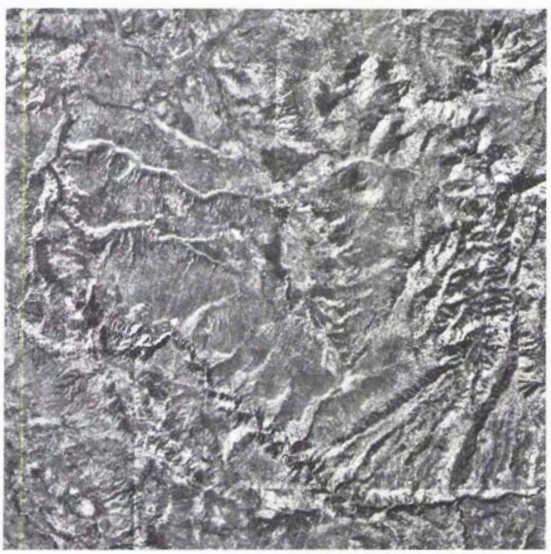

FIG. 4. Image displaying M_T, which is the image brightness distribution in which tone variation is uniquely identified with slope. Landsat scene same as that of Figure 1.

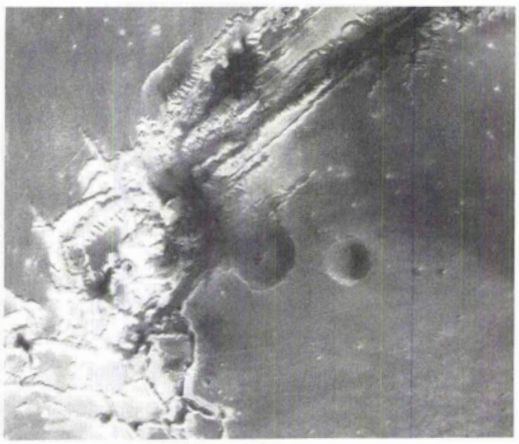

(a)

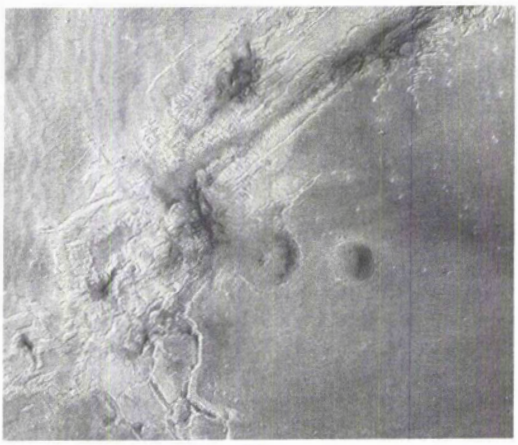

(b)

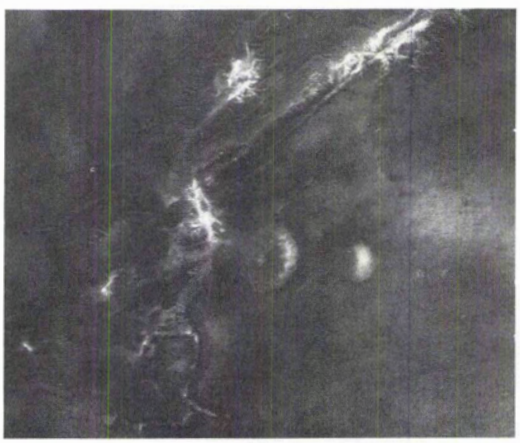

(c)

FIG. 5. Viking Orbiter image of a portion of the Valles Marineris region on Mars (Picture No. 583A24). North is at top. Scale is 0.8 km/pixel. (a) Red spectral component; image array size is 800 by 800 pixels. (b) Red/green band ratio. (c) Violet/green band ratio.

FIG. 6. Estimate of the average scene brightness $R(x,y,\lambda_{red})$, which reflects only the intrinsic properties (albedo and color) of the materials within the scene. Coverage same as that of Figure 5.

PROCESSING LIMITATIONS

The principal sources of error stem from inability in the classification procedure to separate completely the materials. The problem arises primarily from the fact that materials can have similar ratio signatures and different albedo or brightness values. This situation results in mixing two or more materials into one cluster and assigning a value to $\bar{R}_i$ that is the average brightness of a different material. The problem was minimized by dividing the area of the classified image into sections, N by N pixels, and then classifying and computing an average reflectivity map for each image section, rather than producing one map for the entire image-brightness distribution. This procedure greatly reduced the probability of mixing two materials with the same color but different albedo in the classification. The remaining limitation involves selecting a box size small enough to eliminate mixing between albedo units, but large enough to retain sufficient statistics for classification. Selection of a box size of 100 by 100 pixels proved successful for this study; however, the selection of box size is scene dependent and is based entirely on albedo and color variations of surface materials. Faint remnants of these boxes can be seen in Figures 3, 4, 6, and 7. First-order residual seams between image sections were then suppressed on appropriate files (Soderblom *et al.*, 1977).

An additional problem is the existence of peaks of high- or low-density values inconsistent with the values of a cluster (i.e., random noise or bit errors) that may be misclassified and that may subsequently influence average brightness. This problem is solved by excluding data values outside a tolerance defined relative to the overall standard deviation of each cluster.

The problem of confusing local albedo variations with topographically induced brightness variations can exist in areas where the topographic effects are large. (The signal-to-noise ratio is poor when the sun angle is low, creating long shadow lengths.) If the variable haze across an image is extreme (due to local smoke, smog, etc.), the overall average haze solution may not be sufficient, and may leave subtle brightness variations that are falsely interpreted as slope effects.

DATA DISPLAY

The derivation of $\bar{R}_i$ and subsequently of M_T allows the original MS data to be further reduced, generating uncalibrated albedo maps for all bands. In reference to Equation 3, the spectral reflectivity can be written

$$R(x,y,\lambda_i) = \frac{B(x,y,\lambda_i)}{M_T(T,\Phi)} \tag{7}$$

The effect of this band-reduction process is demonstrated by the Landsat band 7 image and the corresponding band 7 albedo map (Figure 8).

Applications of the above process are widespread (e.g., preparation of monochromatic spectral albedo maps and pseudo-topographic base maps for geologic mapping and interpretation). The albedo maps represent the average spectral reflectivity for each material (uniform color and albedo) for each wavelength band, if an essentially "topo-free" or flat surface is assumed. These maps are employed in classification routines in which albedo as well as color ratios are employed. The maps are especially useful in areas of rough topography (with large average slope) where true spectral reflectivity is maksed by intermittent shadow. The topographic component M_T represents, in ef-

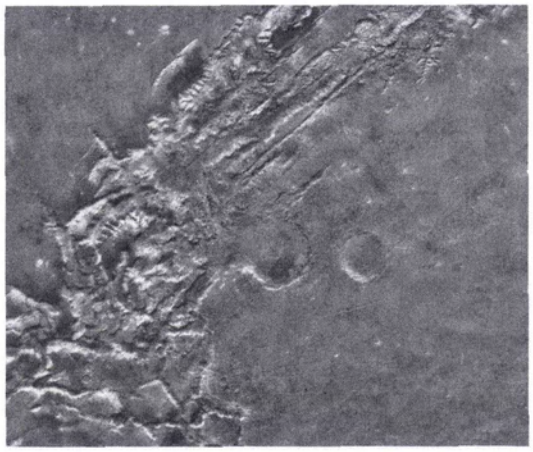

FIG. 7. An estimate of the topographic modulation component, using Figure 6 and the red band. Coverage same as that of Figure 5.

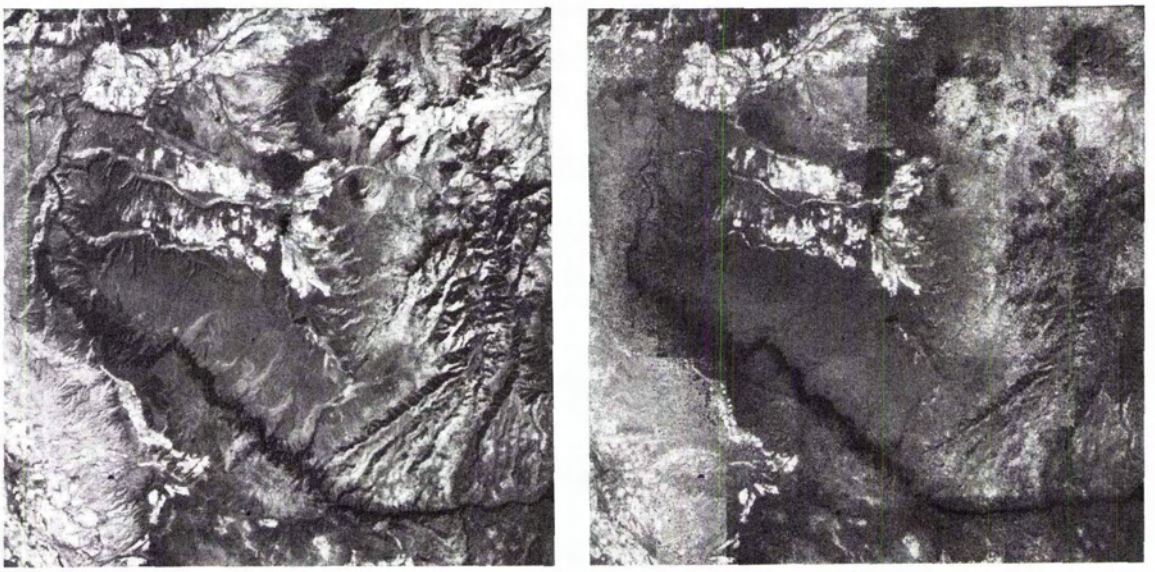

(a) (b)

FIG. 8. Data reduction of band 7 (photographic IR). Landsat scene same as that of Figure 1. (a) Original image. (b) Corresponding band 7 spectral albedo map. This image is essentially free of topography but includes both brightness and spectral information and represents the average spectral reflectivity for each material (uniform color and albedo) in band 7.

fect, a shaded-relief map of the local scene. The low-contrast map in which tone variation is due primarily to slope is more interpretable for topography-related applications.

INTEGRATION OF DIGITAL TOPOGRAPHY

Local, relative height information can be obtained from the topographic component by integrating. We have employed a simple procedure, using a Lambert function:

$$M_T = \cos(\theta - i)/\cos(i) \tag{8}$$

where i is the incidence on a flat surface and θ is the local slope. Although the resultant topography is in fact two dimensional, integration of the topographic profiles is done in one dimension, sum-

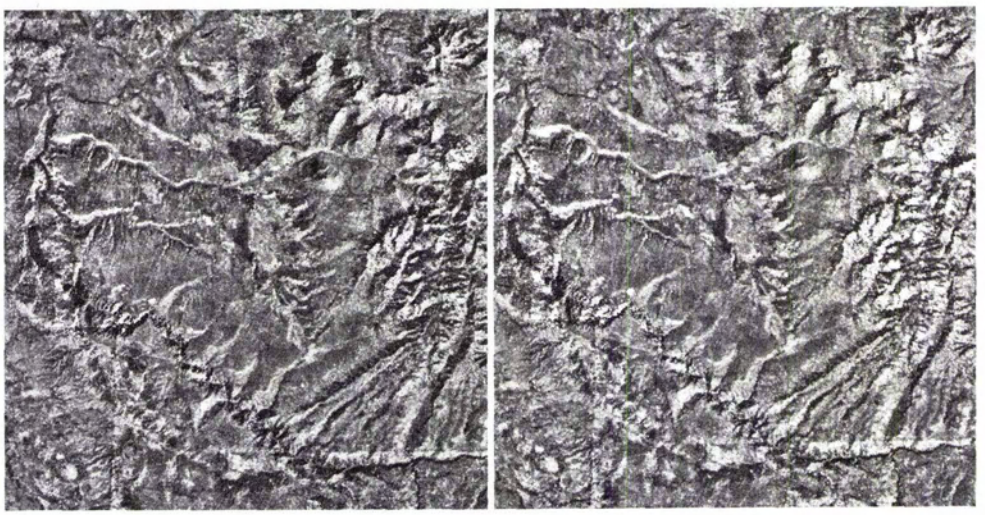

FIG. 9. Stereoscopic display of topographic modulation. A stereogram is generated by combining the topographic modulation (Figure 4) and the local, relative height information obtained by integrating the slope component. Landsat scene essentially same as that of Figure 1.

ming down one image line at a time and considering only brightness variation down range (down sun). More sophisticated integration schemes can be used that explicitly take into account cross-sun topography; however, such schemes are not uniquely determinate (Wildey, oral commun., 1980). For the computation process, the picture is rotated so that the sun azimuth is in the down-line direction, and the incidence angle is positive for west lighting; all slopes are assumed to be less than the angle of incidence. Operating on Equation 8, θ is found from

$$\sin(\theta) = \frac{M_T \tan(i) \pm \sec^2(i) - M_T^2}{\sec^2(i)} \quad \text{where } |\theta| < |i|, \tag{9}$$

and from θ we compute the component of slope, $T(x,y)$, for each point in the image. $\Delta x * \tan\theta$ is computed for every pixel, where Δx is the pixel spacing. The process uses a look-up table where image brightness is plotted versus slope. The relative height values are computed on the basis of the actual local sun elevation and the pixel spacing (i.e., 79 meters for Landsat data).

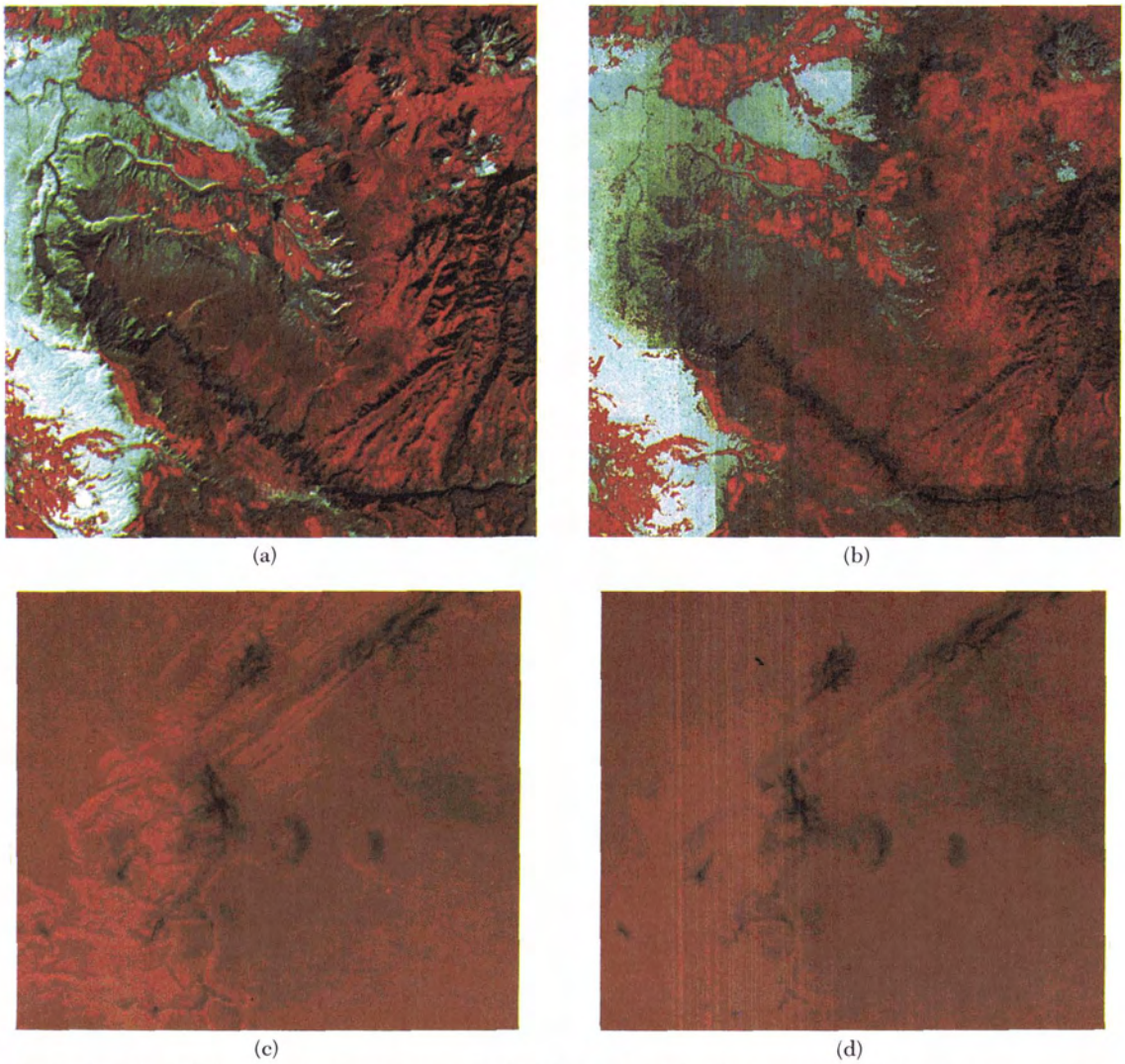

PLATE 1. (a) IR (false color) composite image showing part of the drainage area of the Gunnison River, Colorado. Portion of Landsat scene 1407-17190, acquired 13 September 1973. North is at top. Image array is 1000 by 1000 pixels; scale is 80 m/pixel. (b) Corresponding IR color image in which the average spectral reflectivity maps of bands 4, 5, and 7 were composited to enhance color and albedo variations. (c) Natural color composite of a Viking Orbiter image showing a portion of the Valles Marineris region on Mars. Picture numbers: 583A18 (Violet), 583A22 (Green), and 583A24 (Red). North is at top. Image array is 800 by 800 pixels; scale is 0.8 km/pixel. (d) Corresponding natural color composite displaying only the intrinsic properties (color and albedo) of the materials within the scene.

Combining the topographic modulation M_T and the corresponding slope component $T(x,y)$, a synthetic stereopair of the scene can be generated. Parallax is introduced into the topographic component as a linear function of the relative height defined at each point in the image. The model replots the pixels into the left image of the stereopair, which has the desired relief displacement and vertical exaggeration (Batson *et al.*, 1976). A synthetic stereogram can be generated for photo interpretation displaying only the local topographic modulation (a stereoscopic display of a monoscopic topography map without color variation) (Figure 9).

OTHER APPLICATIONS

Conventional, multivariable, image-processing enhancement can be applied to the albedo data to produce such products as false-color maps, simulated natural-color maps, band ratios, and various color hybrid displays, all without topographic effects. Two examples are the color composites in Plate 1.

A side product derived from this investigation was the development of an alternate spectral-classification image in which the albedo component R (topography removed) is combined in a color composite with the two condensed ratio variables, r_{65} and r.

Conclusion

A technique has been developed to separate and extract spectral reflectivity variations and topographic information from multispectral image data from systems of close wavelengths. The most significant advantage of the technique is that it is a closed system, employing only the multispectral data and limited only by the ability to classify spectral-reflectivity variations in a local area. The technique can be applied to any multispectral data set.

Although the imaged albedo is no more than an approximation to scaled albedo, it is confidently a monotonic function of the true normal albedo across fairly large areas. The essentially "topo-free" data can be used in classification of material types for geologic mapping and interpretation and in land-use and in land-management operations. In turn, the imaged topography (the low-contrast, "shaded-relief" map) and the subjective stereoscopic display provide useful local, relative height information across the image.

Acknowledgments

This research was sponsored by the Earth Resources Observations Systems (EROS) Program and by the Geologic Division, U.S. Geological Survey, both of the Department of Interior.

References

Batson, R. M., K. Edwards, and E. M. Eliason, 1976. Synthetic stereo and Landsat pictures: *Photogrammetric Engineering and Remote Sensing*, V. 42, no. 10, pp. 1279-1284.

Benesh, M., and T. Thorpe, 1976. *Viking Orbiter 1975 visual imaging subsystem calibration report:* Jet Propulsion Laboratory, California Institute of Technology, Pasadena, California, Document No. 611-125.

Bonner, W. J., and R. A. Schmall, 1973. *A photometric technique for determining planetary slopes from orbital photographs*: U.S. Geological Survey Prof. Paper 812A, pp. A1-A16.

Chavez, P. S., 1975. Atmospheric, solar, and MTF correction for ERTS digital imagery (abs.): American Society of Photogrammetry, *Proceedings*, Phoenix, Arizona meeting, October 1975, pp. 69-69a.

Hapke, B. W., 1963. A theoretical photometric function for the lunar surface: *J. Geophys. Res.*, V. 68, pp. 4571-4586.

Hapke, B. W., 1966. An improved theoretical lunar photometric function: *Astron. J.*, V. 71, pp. 333-339.

Lucchitta, B. K., and N. A. Gambell, 1969. Evaluation of photoclinometric profile derivations: in *Analysis of Apollo 8 photography and visual observations*, National Aeronautics and Space Administration Spec. Pub.-201, pp. 51-59.

National Aeronautics and Space Administration, 1976. *Landsat data users handbook*, NASA Document No. 76SPS4258.

Rowan, L. D., J. F. McCauley, and E. A. Holm, 1971. *Lunar terrain mapping and relative roughness analysis*: U.S. Geological Survey Prof. Paper 599G, pp. G1-G32.

Soderblom, L. A., K. Edwards, E. M. Eliason, E. M. Sanchez, and M. P. Charette, 1977. Global color variations on the martian surface, *Icarus*, V. 34, pp. 446-464.

Taranik, J. Y., 1978. *Characteristics of the Landsat multi-spectral data system*: U.S. Geological Survey Open-File Report 78-187, 75p.

Watson, K., 1968. *Photoclinometry from spacecraft images*: U.S. Geological Survey Prof. Paper 599B, pp. B1-B10.

Wildey, R. L., 1971. Limited-interval definitions of the photometric functions of lunar crater walls by photography from orbiting Apollo: *Icarus*, V. 15, pp. 93-99.

———, 1975. Generalized photoclinometry for Mariner 9: *Icarus*, V. 75, pp. 613-626.

Wildey, R. L., and H. A. Pohn, 1964. Detailed photoelectric photometry of the Moon: *Astron. J.*, V. 69, pp. 619-634.

———, 1969. The normal albedo of the Apollo 11 landing site and intrinsic dispersion in the lunar heiligenschein: *Astrophys. J.*, V. 158, pp. L129-L130.

(Received 3 December 1980; accepted 9 May 1981)